

# *How do ultra-low frequency waves access the inner magnetosphere during geomagnetic storms?*

Article

Accepted Version

Rae, I. J., Murphy, K. R., Watt, C. E. J., Sandhu, J. K., Georgiou, M., Degeling, A. W., Forsyth, C., Bentley, S. N., Staples, F. A. and Shi, Q. (2019) How do ultra-low frequency waves access the inner magnetosphere during geomagnetic storms? *Geophysical Research Letters*, 46 (19). pp. 10699-10709. ISSN 0094-8276 doi: 10.1029/2019GL082395

Available at

<https://reading-pure-test.eprints-hosting.org/83939/>

It is advisable to refer to the publisher's version if you intend to cite from the work. See [Guidance on citing](#).

To link to this article DOI: <http://dx.doi.org/10.1029/2019GL082395>

Publisher: American Geophysical Union

All outputs in CentAUR are protected by Intellectual Property Rights law, including copyright law. Copyright and IPR is retained by the creators or other copyright holders. Terms and conditions for use of this material are defined in the [End User Agreement](#).

[www.reading.ac.uk/centaur](http://www.reading.ac.uk/centaur)

**CentAUR**

Central Archive at the University of Reading

Reading's research outputs online

1           **How do Ultra-Low Frequency waves access the inner magnetosphere during**  
2           **geomagnetic storms?**

3           **I. Jonathan Rae,<sup>1</sup> Kyle R. Murphy,<sup>2</sup> Clare E. J. Watt,<sup>3</sup> Jasmine K. Sandhu,<sup>1</sup> Marina**  
4           **Georgiou,<sup>1</sup> Alex W. Degeling,<sup>4</sup> Colin Forsyth,<sup>1</sup> Sarah N. Bentley,<sup>3</sup> Frances A. Staples,<sup>1</sup>**  
5           **Quanqi Shi<sup>4</sup>**

6           <sup>1</sup>Mullard Space Science Lab, UCL, UK

7           <sup>2</sup>University of Maryland, USA

8           <sup>3</sup>University of Reading, UK

9           <sup>4</sup>Shandong University, China

10

11           Corresponding author: Jonathan Rae ([jonathan.rae@ucl.ac.uk](mailto:jonathan.rae@ucl.ac.uk))

12           **Key Points:**

- 13           • We determine the Alfvén continuum and enhancement of global Ultra-Low Frequency  
14           (ULF) waves during the 2013 St. Patrick's Day geomagnetic storm
- 15           • When the Alfvén continuum plummets, lower frequency waves are able to penetrate far  
16           deeper into the magnetosphere than expected
- 17           • Both solar wind and internal geomagnetic conditions must be considered for the  
18           penetration of ULF waves into the inner magnetosphere.

20 **Abstract**

21 Wave-particle interactions play a key role in radiation belt dynamics. Traditionally, Ultra-Low  
22 Frequency (ULF) wave-particle interaction is parameterised statistically by a small number of  
23 controlling factors for given solar wind driving conditions or geomagnetic activity levels. Here,  
24 we investigate solar wind driving of ultra-low frequency (ULF) wave power and the role of the  
25 magnetosphere in screening that power from penetrating deep into the inner magnetosphere. We  
26 demonstrate that, during enhanced ring current intensity, the Alfvén continuum plummets,  
27 allowing lower frequency waves to penetrate deeper into the magnetosphere than during quiet  
28 periods. With this penetration, ULF wave power is able to accumulate closer to the Earth than  
29 characterised by statistical models. During periods of enhanced solar wind driving such as  
30 coronal mass ejection driven storms, where ring current intensities maximise, the observed  
31 penetration provides a simple physics-based reason for why storm-time ULF wave power is  
32 different compared to non-storm time waves.

33 **Plain Language Summary**

34 Geomagnetic storms are the most dynamic and unpredictable phenomena in near-Earth space.  
35 During geomagnetic storms, the Van Allen Radiation Belts can be significantly enhanced, via a  
36 number of physical processes. One of these processes is the action of large-scale Ultra-Low  
37 Frequency (ULF) waves which are in large part directly related to the prevailing solar wind  
38 conditions. In this study, we show that the conditions and internal structuring in near-Earth  
39 space during a geomagnetic storm dictate how close to the Earth these large-scale waves can  
40 reach. Through a combination of ground-based and in-situ measurements, we show how  
41 magnetic field strength and heavy ions control where these waves can access. We show that  
42 conditions both internal and external to near-Earth space must be taken into account to  
43 understand the behavior of waves, and therefore radiation belt particle dynamics, during  
44 geomagnetic storms.

45

46 **1 Introduction**

47 To provide a physically sound basis for models of energetic, relativistic electron dynamics (with  
48 energies >500 keV) in the radiation belts, the balance between acceleration, transport and loss  
49 processes must be known. Electromagnetic waves across a large range of frequencies mediate  
50 the energy transfer processes in the plasma through a myriad of wave-particle interactions. This  
51 is especially true during geomagnetic storms, where the electrons in the radiation belt and the  
52 electromagnetic waves shaping their dynamics are at their most variable (Murphy et al., 2016;  
53 Watt et al., 2017).

54 Very Low Frequency (VLF) chorus waves play a fundamental role in radiation belt electron  
55 dynamics driving loss to the upper atmosphere (O'Brien et al., 2004) and acceleration within the  
56 heart of the outer radiation belt (Reeves et al., 2013). These waves are a critical process for  
57 modeling storm-time dynamics of the outer radiation belt (Thorne et al., 2013). Electromagnetic  
58 ion cyclotron (EMIC) and VLF hiss waves are largely associated with rapid and slow loss from  
59 the radiation belts respectively (Loto'aniu et al., 2006; Thorne et al., 2013). ULF waves transport  
60 and energize electrons via discrete resonances (e.g., Mann et al., 2013) and diffusive radial  
61 transport (e.g. Falthammar, 1965).

62 Recent work demonstrated both ULF and VLF waves are highly variable during storms and  
63 poorly characterized by empirical wave models (e.g., Ma et al., 2018; Murphy et al., 2016; Tu et  
64 al., 2013; Watt et al., 2017). For instance, Tu et al. (2013) have shown that event-specific VLF  
65 chorus diffusion coefficients can be two orders of magnitude larger than to those derived from  
66 empirical models. Murphy et al. (2016) demonstrated that storm-time ULF wave power is highly  
67 variable and can be several orders of magnitude larger than that predicted by empirical wave  
68 models.

69 It is not well understood why differences should exist between storm-time and non storm-time  
70 waves. The basic concept of MHD wave propagation in the magnetosphere is that, for a given  
71 wave frequency, its penetration is determined by the background magnetic field profile, the mass  
72 density and azimuthal wavenumber (Lee, 1996; Figure 4). MHD waves will partially reflect and  
73 the wave power will evanesce where the MHD wave mode reaches a turning point (i.e. the cut-  
74 off frequency exceeds the wave frequency). The fundamental mode eigenfrequency lies  
75 earthward of the turning point. Consequently, the global eigenfrequency configuration is  
76 indicative of how deeply ULF wave power of a given frequency and wavenumber can access the  
77 inner magnetosphere. Here, we investigate a storm occurring during the Van Allen Probe era, to  
78 determine why storm-time ULF wave power may be so different than statistical norms.

79 **2 2013 St Patrick's Day Storm**80 **2.1 General Overview**

81 The 2013 St. Patrick's Day storm forms one of the radiation belt challenge events from the  
82 Quantitative Assessment of Radiation Belt Modeling focus group of the Geospace Environment  
83 Modeling (GEM) program (<http://bit.ly/28UnLpw>) that has already been remarkably well studied  
84 in the literature (e.g., Albert et al., 2018; Engebretson et al., 2018; Ma et al., 2018). Figure S1

85 shows an overview of the solar wind and magnetospheric observations from 15-21 March 2013  
86 inclusive and the overview of the event.

87        2.2 Background Alfvén Continuum

88 ULF waves generated at the magnetopause as a result of the interaction of the Earth's  
89 magnetosphere with the solar wind are reflected and refracted as they approach the inner  
90 magnetosphere by the Alfvén continuum (e.g., Mathie et al., 1999). The Alfvén continuum  
91 determines how deep fast mode waves with a specific frequency may propagate into the  
92 magnetosphere from the magnetopause. ULF waves generated at the magnetopause propagate  
93 radially inwards without generally losing energy. The Alfvén continuum determines the location  
94 at which the fast mode would enter the evanescent regime, and at which point the fast mode can  
95 couple to the Alfvén mode and drive toroidal-mode field line resonances (FLRs) (Samson et al.,  
96 1971).

97 It is difficult to determine the global Alfvén continuum from space-based measurements, however  
98 this is routinely possible for the dayside hemisphere from ground-based magnetometer  
99 measurements (e.g., Waters et al., 1991). Cross-phase analysis can determine the fundamental  
100 resonant eigenfrequency between two magnetometer stations (Supplementary material S2) and  
101 we use the CARISMA (Canadian Array for Realtime Investigations of Magnetic Activity; Mann  
102 et al., 2008) array, using the technique documented by Sandhu et al. [2018a].

103 Figure 1 shows the results of this automated cross-phase analysis. Each panel displays the  
104 median field line eigenfrequency as a function of L-shell, separated into dawn sector (0600-1200  
105 MLT, solid lines) and dusk sectors (1200-1800MLT, dashed lines) for each of the days of 15-21  
106 March 2013 inclusive.

107 Field line eigenfrequencies are dependent upon the length of, and Alfvén velocity along, a given  
108 field line. During normal conditions, the eigenfrequency decreases monotonically with radial  
109 distance in regions inside and outside the plasmapause because the dominant magnetic field  
110 strength decays and field line lengths increase. Across the plasmapause, the plasma density drops  
111 sharply with radial distance, and the eigenfrequency will increase with radial distance over a  
112 short span of L (see Figure F1, Kale et al., 2007).

113 On 15 March 2013, the Alfvén eigenfrequency continuum displays the same behavior described  
114 above, with a small plasmapause reversal between  $L = 4.2 - 4.3$  in the dusk sector. During 16  
115 March 2013, the eigenfrequency profile is highly variable, at increased or similar frequencies  
116 across all L-shells in the dawn sector. In the dusk sector, eigenfrequencies decrease slightly at  
117 low-L and increase sharply at  $L \sim 5$ , which may indicate the presence of a plasmaspheric plume.

118 On 17 March 2013, however, there is little evidence of any increasing plasmapause gradient in  
119 the continuum across all L and the eigenfrequencies have reduced across all L-shells outside  $L =$   
120 3.4. There is some evidence of an MLT asymmetry; that dawn eigenfrequencies are higher than  
121 those at dusk. This reduction in the Alfvén continuum is concurrent with the arrival of the CME  
122 and the initiation of this geomagnetic storm around 0500 UT.

123 On 18 March 2013, there are still some dawn-dusk differences in eigenfrequency profiles inside  
124 of  $L = 4.2$ , whereby dawn frequencies are up to 50% higher than their dusk counterparts. All

125 eigenfrequencies inside of L~5 are also higher than their counterparts on the previous day. Both  
126 increases in eigenfrequencies and asymmetries in the plasmaspheric density are consistent with  
127 the presence of the remnants of a plasmaspheric density plume of the previous day (e.g.,  
128 Borovsky and Denton, 2008).

129 On 19 March 2013, the eigenfrequency profiles return to similar values as 17 March 2013, and  
130 the differences between the dawn and dusk asymmetries have reduced. Towards the end of the  
131 period examined, on 20 and 21 March 2013, significant MLT and L-shell variations are found.  
132 The eigenfrequency profiles are very different in each MLT sector, and the eigenfrequency  
133 values at around L=5 are much larger than they were on 19 March 2013. These major changes  
134 are coincident with the arrival of the secondary CME (see previous section) at around 1200 on 20  
135 March 2013. We discuss these changes in the eigenfrequency profile in terms of plasma density  
136 evolution through the two consecutive geomagnetic storms.

### 137 2.3 Storm-time ULF wave power

138 We take the vector summed power from the CARISMA (Mann et al., 2008) and IMAGE (Lühr,  
139 1994) magnetometer networks throughout the storm across 51 magnetometers in the same  
140 manner as Murphy et al. (2015; 2016) and Mann et al. (2015) and limit our analysis to the  
141 dayside hemisphere only and compare this with Figure 1. We limit the analysis to the dayside  
142 such that the powers are not influenced by substorm activity (Murphy et al., 2011; Rae et al.,  
143 2011).

144 We use 51 magnetometers to calculate the summed ULF power between 0.83-15.83 mHz at 1  
145 hour resolution throughout the storm period and interpolated onto a uniform 2D grid (original  
146 data - Supplementary Material S3).

147 Figure 2 (top) shows the results of this ground-based analysis of summed ULF wave power as a  
148 function of L and time from 15-22 March 2013. Clear from Figure 2 (top) is that the ULF wave  
149 activity is highly time-dependent during the period of interest. The ULF wave power across the  
150 storm varies both in strength and in penetration depth into the magnetosphere and across multiple  
151 frequencies (see Supplementary Material S4).

152 There are also interesting ULF wave signatures at other times that can be associated with other  
153 solar wind drivers. Two enhancements in ULF wave power across all L are seen early on 15  
154 March 2013 and the morning of 16 March 2013. Using the statistical results of Bentley et al.  
155 (2018) as an aid, the ULF wave power enhancements on the morning of 15 March 2013 are  
156 likely related to the large change in plasma density and negative IMF Bz seen in the solar wind.  
157 A similar negative IMF Bz deflection accompanied by a smaller change in plasma density are  
158 also seen on the morning of 16 March 2013. Prior to the CME arrival (17 March 2013), the ULF  
159 wave activity was quiet and significant ULF wave power ( $10 \text{ nT}^2/\text{mHz}$ ) was not seen any further  
160 inside the magnetosphere than L~6. However, on arrival of the CME, the ULF waves are  
161 enhanced across all L-shells, the power increasing to  $>10^3 \text{ nT}^2/\text{mHz}$  at high L, and reaching  
162  $10^2 \text{ nT}^2/\text{mHz}$  at L=3. The increase in ULF wave activity at high L is likely associated with the  
163 significant increase in solar wind velocity and negative IMF Bz that accompany the start of the  
164 CME, but what is most interesting is just how far inside the magnetosphere the increase in ULF  
165 wave power is seen.

166 In the ensuing recovery phase on 18 March 2013, the ULF wave power reduces in strength  
167 across all locations. Interestingly, the wave amplitude at high L is fairly constant throughout 18  
168 March and into the morning of 19 March 2013. However, the wave activity increases abruptly at  
169 lower L in the early hours of 19 March 2013 before decreasing again to a background level a few  
170 hours later.

171 Finally, on the morning of the 21 March 2013, ULF wave power is once again enhanced,  
172 reaching  $103 \text{ nT}^2/\text{mHz}$  at high L, and  $>101 \text{ nT}^2/\text{mHz}$  at L=3, presumably due to the arrival of the  
173 second CME with its increase in solar wind velocity and subsequent ULF energization. We  
174 discuss the role of external driving and internal background Alfvén continuum in this  
175 energization below.

176 Figure 2 (bottom) shows a 2D interpolation of the results shown in Figure 1 of the Alfvén  
177 continuum as a function of L-shell and time where colour indicates frequency. A similar type of  
178 interpolation has been performed as in the top panel, with a 6 hour time scale, and 0.5 L spatial  
179 scale. Overplotted on Figure 2 (bottom) are isocontours of specific frequencies (5, 7 and 9 mHz)  
180 to highlight the variability of the location of a particular eigenfrequency over the course of the  
181 interval.

182 Figure 2 (bottom) shows that there is significant structuring of the Alfvén continuum as a  
183 function of L and time. Specifically, if we consider the propagation of ULF waves inwards  
184 through the magnetosphere, then the continuum structure prior to the storm (i.e. on 15 and 16  
185 March 2013) would enable ULF wave energy at high frequencies ( $>10\text{mHz}$ ) to access the inner  
186 magnetosphere, but frequencies lower than that would be reflected and refracted or evanesce.  
187 However, once the storm main phase has commenced, the eigenfrequency profile reduces  
188 dramatically, such that wave frequencies of 5 mHz could propagate into the inner magnetosphere  
189 without hindrance. The 9 mHz contour moves in to L<3.5 after the storm modifies the  
190 magnetosphere, as compared to the period prior to the storm where the 9 mHz contour exists at  
191 L>5. Figure S4 shows ULF wave power at these specific frequencies of 5, ~7 and ~9 mHz, and  
192 demonstrates that the ULF wave power at given frequencies does indeed penetrate to lower-L  
193 when the eigenfrequency continuum is suppressed.

194 As the storm moves into the recovery phase, the ULF wave power in Figure 2 (top) wanes at  
195 higher L-shells, at the same time as the Alfvén continuum relaxes, such that 5 mHz contours are  
196 now around L=6. On 19 March 2013, the Alfvén continuum again reduces to a storm-like level,  
197 and we observe another ULF wave penetration event (Figure 2 (top)). Finally, Figure 2 (bottom)  
198 shows that towards the end of the interval, at the same time as the second, smaller storm, the  
199 pattern of the eigenfrequency continuum is reversed such that low frequencies are observed at  
200 low L and vice versa. We conclude that either the plasmapause is around L~4 and the  
201 eigenfrequency continuum returns to a more typical profile (c.f., Figure 1, Kale et al., 2007) or  
202 that there may be a complicated Alfvén continuum due to the recovery phase of one storm  
203 coinciding with another.

### 204 **3 Discussion and Conclusions**

205 ULF waves are a key component of any storm-time study of relativistic electron dynamics,  
206 whether they are responsible for direct energization (Claudpierre et al., 2013), transport (Mann et

207 al., 2015; Ozeke et al, 2018), or losses (e.g., Rae et al., 2018). Here, we investigate the role of  
208 ULF waves during a geomagnetically active period, with the critical addition of using the  
209 eigenfrequency continuum to monitor the changes in the internal environment of the  
210 magnetosphere, as seen by the ULF waves.

211 It is now established that the main source of global-scale ULF wave power is the solar wind.  
212 Global-scale ULF waves have low azimuthal wavenumbers,  $m$ , the value of which describes the  
213 number of wavelengths around the Earth at a given radial distance. Solar wind speed (Mathie  
214 and Mann, 2001; Murphy et al., 2011; Rae et al., 2012) and dynamic pressure (Kepko et al.,  
215 2002; Sibeck et al., 1989) have both been studied as controlling factors. However, the  
216 interdependence of solar wind parameters can often mask the underlying factors that result in  
217 enhanced ULF wave power, necessitating a systematic statistical study. Recently, the relative  
218 contributions of solar wind drivers of ULF wave power have been quantified by Bentley et al.  
219 (2018). In this work, Bentley et al. (2018) found that solar wind speed was the dominant driver,  
220 followed by the southward component of IMF Bz and, in contrast to previous work, the variance  
221 in number density, as opposed to the derived dynamic pressure. Statistically, as solar wind  
222 driving enhances, ULF wave power increases monotonically at all radial distances in the inner  
223 magnetosphere (e.g., Georgiou et al., 2018; Mathie et al., 1999; Rae et al., 2012). However,  
224 none of these previous statistical studies take into account the time history of the solar wind,  
225 including the temporal behavior of CMEs, corotating interaction regions (CIRs) or other solar  
226 wind transients. Hence, the time-dependent nature of the solar wind may be a critical missing  
227 factor in empirical models of solar wind driven ULF wave activity.

228 Equally, the internal plasma conditions of the magnetosphere are typically not considered in  
229 parameterized models of ULF wave power. Such models often use a geomagnetic index as a  
230 proxy for the external solar wind driving and internal magnetospheric dynamics (e.g. the K<sub>p</sub>  
231 model of Ozeke et al., (2014)). Physically, ULF wave activity in the magnetosphere is dictated  
232 by the background magnetic field strength and the number density and composition of the cold  
233 plasma. It is these parameters that control the Alfvén eigenfrequency profile and hence the  
234 accessibility of ULF wave power into a given magnetospheric location.

235 Figure 1 shows the variation of the Alfvén continuum with L-shell, frequency and time  
236 throughout the 2013 St. Patrick's Day storm. During the storm main phase, the Alfvén  
237 continuum is suppressed at the vast majority of L-shells, other than around L=3.4 where there is  
238 some evidence of a newly formed or refilling plasmapause. The consequence of this is that  
239 prior to the storm, only frequencies greater than 12 mHz could access the inner magnetosphere  
240 without evanescently decaying. During the main phase of the storm, suddenly any frequencies  
241 greater than 5 mHz can now penetrate into the inner magnetosphere as deep as L=3.4.

242 During this storm, the ULF wave power (Figure 2 (top)) is highly dynamic, varying by 3 orders  
243 of magnitude. Storm-time ULF wave power has been shown to be significantly variable during  
244 the main phase of the storm (e.g., Loto'aniu et al., 2006; Murphy et al., 2016). During one of the  
245 largest geomagnetic storms in recent history, the "Halloween storm" of 2003, Loto'aniu et al.  
246 (2006) found that ULF wave power varied by 4 orders of magnitude. Interestingly these authors  
247 also found that ULF wave power was most enhanced during the two storm main phases. More  
248 specifically, the largest ULF wave power during the Halloween storm occurred during the three  
249 periods of increasingly negative Dst index.

250 During periods where the eigenfrequencies are lower, ULF wave power reaches deeper into the  
251 magnetosphere (Figure 2). ULF wave power inside the magnetosphere has a power law like  
252 power spectrum (Bentley et al., 2018; Rae et al., 2012). Hence, when lower frequencies can  
253 access lower L-shells, the summed ULF wave power is generally higher. When the Alfvén  
254 profile recovers between 19-20 March 2013, ULF wave power is screened from the inner  
255 magnetosphere. However, when the second geomagnetic storm occurs on the 20 March 2013,  
256 ULF wave power again accesses the inner magnetosphere. By inspection of Figure 1 and Figure  
257 2, it is clear that the eigenfrequency variations are complex, but this may result in plasmaspheric  
258 plumes significantly complicating the simple ULF wave dynamics that are described in the  
259 current literature. Essentially, when there are both radial and azimuthal gradients in the Alfvén  
260 continuum, there is a frequency dependent accumulation and penetration of ULF wave power  
261 through, and indeed within, the plume (c.f., Figure 3(a), Degeling et al., 2018), which will  
262 complicate the magnetospheric location of ULF wave powers.

263 The natural eigenfrequency of geomagnetic field lines is determined by its magnetic field profile  
264 and the mass density along the field line. During geomagnetic storms, it is usually thought that  
265 heavy ion outflow increases the mass density sufficiently to lower the Alfvén continuum (e.g.,  
266 Engwall et al. 2009; Kale et al., 2009; Kronberg et al., 2014; Loto’aniu et al., 2006; Yau et al.,  
267 1988). Certainly heavy ions must play a role. However, Sandhu et al (2018b) constructed a  
268 statistical model of the average mass densities as a function of Dst index. Sandhu et al. (2018b)  
269 found that, although the average ion mass did increase significantly with increasingly negative  
270 Dst index, the electron densities in the inner magnetosphere reduced.

271 Hence on average, lower Dst index values reduce the plasma mass density, rather than increasing  
272 it as previously thought. Sandhu et al. (2018b) concluded that the changes in the magnetic field  
273 drove the changes in eigenfrequency; during sudden increases in dayside compression, the  
274 geomagnetic field strength in the outer magnetosphere increases across the dayside. It is  
275 important to remember that when using a proxy such as Dst index, two very different intervals  
276 are averaged, decreasing Dst during the main phase and increasing Dst during the recovery phase  
277 even though both phases pass through the same values of Dst. However, Sandhu et al.’s (2018b)  
278 model provides useful context for interpreting our results. We now consider the role of the ring  
279 current itself in reducing the Alfvén continuum in the inner magnetosphere. Commonly, the “Dst  
280 effect” (Kim and Chan, 1997) is specifically limited to the effect of ring current enhancement  
281 encouraging electron loss. Here we suggest that the strengthening ring current significantly  
282 changes the Alfvén continuum during key periods of the storm.

283 Relationships between ring current intensity and ULF wave power have been discussed  
284 previously (e.g., Mann et al., 2012; Murphy et al, 2014), suggesting a causal link between ring  
285 current ions and the generation of storm-time high-m waves that could play additional roles in  
286 energization (eg., Ozeke and Mann, 2008) and loss (e.g., Rae et al., 2018). Clearly, it is the  
287 interplay between magnetic field and plasma mass densities that is key during the dynamic  
288 period in main phase of the storm. Figures 2 and 3 (bottom) show that the eigenfrequencies are  
289 suppressed during this storm main phase.

290 In order to reduce the Alfvén continuum across a wide range of L-shells, the magnetic field  
291 strength must reduce, or the mass density must increase, or a combination of both. Figure 3(a)  
292 demonstrates the effect of the ring current in reducing the local magnetic field strength at the

293 Van Allen Probes A and B throughout the storm, by displaying the ratio between the magnetic  
294 field strength observed by Van Allen Probes (Kletzing et al., 2014) relative to the IGRF  
295 (International Geomagnetic Reference Field). Note that there is a clear reduction in the ratio  
296 away from 1.0 in the same manner as Shen et al. (2014) discussed that is mirrored by the  
297 negative enhancement in the Dst index. This implies that the expected magnetic field as  
298 measured by the Van Allen Probes is significantly suppressed during the storm main phase and  
299 in response to the evolving ring current.

300 There are a number of factors at play here, however. Field line eigenfrequencies are influenced  
301 by the magnetic field strength and by plasma mass density along the field. In this paper, we  
302 discuss how the inner magnetosphere could respond differently to geomagnetic storms than the  
303 outer magnetosphere. Ion outflow during geomagnetic storms (e.g., Yau et al., 1988) would  
304 certainly influence the plasma mass density at all locations during the main phase of the storm.  
305 However, there is also a secondary effect, which is that there is also enhanced helium and  
306 oxygen ring current ions in the inner magnetosphere (e.g., Sandhu et al., 2018c). The enhanced  
307 ring current (and its contribution to mass densities) will increase the heavy ion content in the  
308 inner magnetosphere, whilst also reducing the local magnetic field strength at ring current radial  
309 distances (Kim and Chan, 1997; Kronberg et al., 2014). Regardless of which effect is dominant,  
310 these additive effects lead to a net decrease in the Alfvén continuum, allowing deep penetration  
311 of ULF wave power into the inner magnetosphere during periods of increase ring current  
312 intensity. It must be stressed that the amplitude of this ULF wave accessibility is dependent  
313 upon the solar wind driver and, while penetration can occur during ring current enhancements,  
314 large amplitude wave power at low-L will occur during periods of enhanced solar wind driving  
315 and ring current intensities (e.g., Loto'aniu et al., 2006). The plasmapause role on Pc5  
316 penetration has been reported before by Hartinger et al. [2010]. Here, we discuss that multiple  
317 storm-time factors of plasma composition and density, global magnetic field configuration and  
318 the suppression of the inner magnetospheric field by the ring current can depress the Alfvén  
319 continuum.

320 Figure 3(b-e) shows ion data from the Van Allen Probes HOPE (Helium Oxygen Proton  
321 Electron) instruments (Funsten et al., 2013; Spence et al., 2013) during the storm. Figure 3(b-e)  
322 shows (b) H<sub>+</sub>, (c) O<sub>+</sub> energy fluxes as a function of energy and time, and (d) the ratio between  
323 these fluxes. Figure 3(c) shows the increase in both low energy oxygen (<100 eV) on 17 March  
324 2013 at ~12 UT, and the delayed increase of higher energy oxygen (100eV-100keV) later in the  
325 geomagnetic storm from 12 UT on 18 March 2013, and with a slow decay lasting ~1-2 days.  
326 This two-step heavy ion increase is consistent with the sharp increase in ion outflow at the start  
327 of the geomagnetic storm (e.g., Gkioulidou et al., 2019; Kronberg et al., 2014) and the longer-  
328 term penetration of heavy ions convected into the inner magnetosphere from substorms (e.g.,  
329 Sandhu et al., 2018). Figure 3(d) shows the ratio of oxygen to hydrogen as a function of energy,  
330 and (e) summed over energy to demonstrate intervals where the heavy ion content of the ring  
331 current should be considered to be significant; the dashed horizontal line indicating unity. On  
332 17 March, the increase in low energy oxygen and the decrease in low energy hydrogen leads to a  
333 large increase in the ratio. The hydrogen content of the ring current recovers over the course of  
334 the 18 March 2013 and there is an additional higher energy oxygen content which maintains an  
335 elevated ratio as seen in Figure 3(e). The additive effect of reduced magnetic field and two-step  
336 heavy ion content leads to a suppressed Alfvén continuum that is highly variable throughout the  
337 entire storm-time period, enabling mHz frequencies to penetrate the inner magnetosphere as a

338 consequence. We conclude that solar wind driving as well as current internal conditions must  
339 both be considered for realistic storm-time ULF wave conditions in the inner magnetosphere.

340 It is interesting to note that the lowering of the continuum and penetration of ULF wave power is  
341 closely coincident with the time and location of rapid enhancement in MeV electron fluxes  
342 (Figure S1), as both ULF wave power and enhancements occur around  $L=3-3.5$ . Such  
343 penetration may also explain slot region filling during very large storms, where both ULF wave  
344 powers and ring current intensities are largest (Ozeke et al., 2018). What role this ULF wave  
345 power plays in shaping the radiation belt enhancement remains to be seen, but what is clear is  
346 that ULF wave powers must be taken into account during radiation belt modelling of such  
347 enhancements.

348 One of the primary challenges of the Quantitative Assessment of Radiation Belt Morphology  
349 (QARBM) Geospace Environment Modeling (GEM) challenge is to assess the validity of  
350 diffusion coefficients during specific geomagnetic storms. Since the accessibility of ULF wave  
351 power is strongly dependent upon internal geomagnetic conditions, we conclude that the radial  
352 dependence of ULF wave diffusion coefficients will vary significantly during geomagnetic  
353 storms not only on external driving but also critically on internal factors that have not yet been  
354 fully considered.

355

## 356 **Acknowledgments**

357 This research was supported by the Natural Environment Research Council (NERC) Highlight  
358 Topic Grant Rad-Sat, and grant numbers NE/P017185/1 and NE/P017274/1, STFC grants  
359 ST/N0007722/1 and ST/R000921/1. C.F. is supported by a NERC IRF NE/N014480/1.

360 All data publically available via [www.carisma.ca](http://www.carisma.ca), <http://space.fmi.fi/image/www/index.php?>.  
361 <http://cdaweb.gsfc.nasa.gov> and <http://rbspgway.jhuapl.edu/psd>

362

363 **References**

364 Albert, J. M., Selesnick, R. S., Morley, S. K., Henderson, M. G., & Kellerman, A. C. (2018).  
365 Calculation of last closed drift shells for the 2013 GEM radiation belt challenge events. *Journal*  
366 *of Geophysical Research: Space Physics*, 123, 9597–9611.  
367 <https://doi.org/10.1029/2018JA025991>

368 Bentley, S. N., Watt, C. E. J., Owens, M. J. and Rae, I. J. (2018) ULF wave activity in the  
369 magnetosphere: resolving solar wind interdependencies to identify driving mechanisms. *Journal*  
370 *of Geophysical Research: Space Physics*, 123 (4). pp. 2745-2771. ISSN 2169-9402 doi:  
371 10.1002/2017ja024740

372 Berube, D., M. B. Moldwin, and J. M. Weygand (2003), An automated method for the detection  
373 of field line resonance frequencies using ground magnetometer techniques, *J. Geophys. Res.*,  
374 108, 1348, doi:10.1029/2002JA009737, A9.

375 Blake, J.B., Carranza, P.A., Claudepierre, S.G. et al. *Space Sci Rev* (2013) 179: 383.  
376 <https://doi.org/10.1007/s11214-013-9991-8> Claudepierre, S. G., et al. (2013), Van Allen Probes  
377 observation of localized drift resonance between poloidal mode ultra-low frequency waves and  
378 60 keV electrons, *Geophys. Res. Lett.*, 40, 4491–4497, doi:10.1002/grl.50901.

379 Degeling, A. W., Rae, I. J., Watt, C. E. J., Shi, Q. Q., Rankin, R., & Zong, Q. -. G. (2018).  
380 Control of ULF Wave Accessibility to the Inner Magnetosphere by the Convection of Plasma  
381 Density. *JOURNAL OF GEOPHYSICAL RESEARCH-SPACE PHYSICS*, 123 (2), 1086-1099.  
382 doi:10.1002/2017JA024874

383 Engebretson, M. J., Posch, J. L., Braun, D. J., Li, W., Ma, Q., Kellerman, A. C., et al. (2018).  
384 EMIC wave events during the four GEM QARBM challenge intervals. *Journal of Geophysical*  
385 *Research: Space Physics*, 123, 6394–6423. <https://doi.org/10.1029/2018JA025505>

386 Engwall, E., A. I. Eriksson, C. M. Cully, M. Andr'e, R. Torbert, and H. Vaith (2009), Earth's  
387 ionospheric outflow dominated by hidden cold plasma, *Nature Geoscience*, pp. 24–27, doi:  
388 10.1038/NGEO387

389 Fälthammar, C.-G. (1965), Effects of time-dependent electric fields on geomagnetically trapped  
390 radiation, *J. Geophys. Res.*, 70(11), 2503–2516, doi:10.1029/JZ070i011p02503.

391 Funsten, H. O., R. M. Skoug, A. A. Guthrie, E. A. MacDonald, J. R. Baldonado, R. H. Harper,  
392 K. C. Henderson, K. H. Kihara, J. E. Lake, B. A. Larsen, A. D. Puckett, V. J. Vigil, R. H. W.  
393 Friedel, M. G. Henderson, J. T. Niehof, G. D. Reeves, and M. F. Thomsen (2013), Helium,  
394 Oxygen, Proton, and Electron (HOPE) Mass Spectrometer for the Radiation Belt Storm Probes  
395 Mission, *Space Science Reviews*, doi:10.1007/s11214-013-9968-7.

396 Georgiou, M., I.A. Daglis, I.J. Rae, E. Zesta, D.G. Sibeck, I.R. Mann, G. Balasis, K. Tsinganios  
397 (2018), Ultra-low frequency waves as an intermediary for solar wind energy input into the  
398 radiation belts, *J. Geophys. Res.*, 123(12), 10,090–10,108

399 Gkioulidou, M., Ohtani, S., Ukhorskiy, A. Y., Mitchell, D. G., Takahashi, K., Spence, H. E., et al  
400 (2019). Low-energy (<keV) O<sup>+</sup> ion outflow directly into the inner magnetosphere: Van Allen  
401 Probes observations. *Journal of Geophysical Research: Space Physics*, 124, 405–419.  
402 <https://doi.org/10.1029/2018JA025862>

403 Hartinger, M., Moldwin, M. B., Angelopoulos, V., Takahashi, K., Singer, H. J., Anderson, R. R.,  
404 Nishimura, Y., and Wygant, J. R. (2010), Pc5 wave power in the quiet-time plasmasphere and  
405 trough: CRRES observations, *Geophys. Res. Lett.*, 37, L07107, doi:10.1029/2010GL042475.

406 Kale, Z.C., I.R. Mann, C.L. Waters, J. Goldstein, F.W. Menk, and L.G. Ozeke (2007), Ground  
407 magnetometer observation of a cross-phase reversal at a steep plasmapause, *J. Geophys. Res.*,  
408 112, A10222, 2007, DOI: 10.1029/2007JA012367.

409 Kale, Z. C., I. R. Mann, C. L. Waters, M. Vellante, T. L. Zhang, and F. Honary (2009),  
410 Plasmaspheric dynamics resulting from the Hallowe'en 2003 geomagnetic storms, *J. Geophys.*  
411 *Res.*, 114, A08204, doi:10.1029/2009JA014194.

412 Kepko, L., H. E. Spence and H. J. Singer (2002), ULF waves in the solar wind as direct drivers  
413 of magnetospheric pulsations, *Geophysical Research Letters*, 29, 1197,  
414 doi:10.1029/2001GL014405

415 Kronberg, Elena A., Maha Ashour-Abdalla, Iannis Dandouras, Dominique C. Delcourt, Elena E.  
416 Grigorenko, Lynn M. Kistler, Ilya V. Kuzichev, Jing Liao, Romain Maggiolo, Helmi V. Malova,  
417 Ksenia G. Orlova, Vahe Peroomian, David R. Shklyar, Yuri Y. Shprits, Daniel T. Welling, Lev  
418 M. Zelenyi (2014), Circulation of Heavy Ions and Their Dynamical Effects in the  
419 Magnetosphere: Recent Observations and Models, *Space Science Reviews*, Volume 184,  
420 Number 1-4, Page 173

421 Lee, D.-H. (1996), Dynamics of MHD wave propagation in the low-latitude magnetosphere, *J.*  
422 *Geophys. Res.*, 101(A7), 15371–15386, doi:10.1029/96JA00608.

423 Loto'aniu, T. M., R. M. Thorne, B. J. Fraser, and D. Summers (2006), Estimating relativistic  
424 electron pitch angle scattering rates using properties of the electromagnetic ion cyclotron wave  
425 spectrum, *J. Geophys. Res.*, 111, A04220, doi:10.1029/2005JA011452.

426 Loto'aniu, T. M., Mann, I. R., Ozeke, L. G., Chan, A. A., Dent, Z. C., & Milling, D. K. (2006).  
427 Radial diffusion of relativistic electrons into the radiation belt slot region during the 2003  
428 Halloween geomagnetic storms. *Journal of Geophysical Research*, 111, A04218. doi:  
429 10.1029/2005JA011355

430 Lühr, H. (1994). The IMAGE magnetometer network, *STEP International* (vol. 4, pp. 4–6).  
431 USSCO.

432 Kim, H.-J., and A. A. Chan (1997), Fully adiabatic changes in storm time relativistic electron  
433 fluxes, *J. Geophys. Res.*, 102, 22,107–22,116, doi:10.1029/97JA01814.

434 Kletzing, C.A., Kurth, W.S., Acuna, M. et al. (2013), The Electric and Magnetic Field  
435 Instrument Suite and Integrated Science (EMFISIS) on RBSP, *Space Sci Rev.*, v. 179, issue 1-4,  
436 127-181.

437 Ma, Q., Li, W., Bortnik, J., Thorne, R. M., Chu, X., Ozeke, L. G., Reeves, G. D., et al. (2018).  
438 Quantitative Evaluation of Radial Diffusion and Local Acceleration Processes During GEM  
439 Challenge Events. *Journal of Geophysical Research (Space Physics)* , 123, 1938-1952.

440 Mann, I. R., Milling, D. K., Rae, I. J., Ozeke, L. G., Kale, A., Kale, Z. C., . . . Singer, H. J.  
441 (2008). The upgraded CARISMA magnetometer array in the THEMIS era. *Space Science  
Reviews*, 141 (1-4), 413-451. doi:10.1007/s11214-008-9457-6#

443 Mann, I. R., Lee, E. A., Claudepierre, S. G., Fennell, J. F., Degeling, A., Rae, I. J., . . . Honary,  
444 F. (2013). Discovery of the action of a geophysical synchrotron in the Earth's Van Allen  
445 radiation belts. *Nature Communications*, 4 (1). doi:10.1038/ncomms3795

446 Mann, I. R., Murphy, K. R., Ozeke, L. G., Rae, I. J., Milling, D. K., Kale, A., & Honary, F.  
447 (2012). The role of ultralow frequency waves in radiation belt dynamics. In D. Summers, I. R.  
448 Mann, D. N. Baker, M. Schultz (Eds.), *Dynamics of the Earth's Radiation Belts and Inner  
449 Magnetosphere* (pp. 69-91). Washington, D.C.: AGU. doi:10.1029/2012GM001349

450 Mann, I. R., Ozeke, L. G., Murphy, K. R., Claudepierre, S. G., Turner, D. L., Baker, D. N., et al.  
451 (2016). Explaining the dynamics of the ultra-relativistic third Van Allen radiation belt. *Nature  
452 Physics*, 12(10), 978–983. <https://doi.org/10.1038/nphys3799>

453 Mathie, R. A., and I. R. Mann (2001), On the solar wind control of Pc5 ULF pulsation power at  
454 mid-latitudes: Implications for MeV electron acceleration in the outer radiation belt, *J. Geophys.  
455 Res.*, 106(A12), 29783–29796, doi:10.1029/2001JA000002.

456 R. A. Mathie F. W. Menk I. R. Mann D. Orr (1999), Discrete Field Line Resonances and the  
457 Alfvén Continuum in the Outer Magnetosphere, *Geophys. Res. Lett.*, doi:  
458 10.1029/1999GL900104

459 Frederick Menk, Zoë Kale, Murray Sciffer, Peter Robinson, Colin Waters, Russell Grew,  
460 Mark Clilverd, Ian Mann (2014), Remote sensing the plasmasphere, plasmapause, plumes and  
461 other features using ground-based magnetometers, *J. Space Weather Space Clim.* 4 A34, DOI:r  
462 10.1051/swsc/2014030

463 Murphy, K. R., Rae, I. J., Mann, I. R., & Milling, D. K. (2011). On the nature of ULF wave  
464 power during nightside auroral activations and substorms: 1. Spatial distribution. *Journal of  
465 Geophysical Research: Space Physics*, 116 (1). doi:10.1029/2010JA015757

466 Murphy, K. R., I. R. Mann, and L. G. Ozeke (2014), A ULF wave driver of ring current  
467 energization, *Geophys. Res. Lett.*, 41, 6595–6602, doi:10.1002/2014GL061253.

468 Murphy, K. R., Mann, I. R., & Sibeck, D. G. (2015). On the dependence of storm time ULF  
469 wave power on magnetopause location: Impacts for ULF wave radial diffusion. *Geophysical  
470 Research Letters*, 42, 9676–9684. <https://doi.org/10.1002/2015GL066592>

471 Murphy, K. R., Mann, I. R., Rae, I. J., Sibeck, D. G., & Watt, C. E. J. (2016). Accurately  
472 characterizing the importance of wave-particle interactions in radiation belt dynamics: The  
473 pitfalls of statistical wave representations. *Journal of Geophysical Research: Space Physics*, 121  
474 (8), 7895-7899. doi:10.1002/2016JA022618

475 O'Brien, T. P., M. D. Looper, and J. B. Blake (2004), Quantification of relativistic electron  
476 microburst losses during the GEM storms, *Geophys. Res. Lett.*, 31, L04802,  
477 doi:10.1029/2003GL018621.

478 Ozeke, L. G., and I. R. Mann (2008), Energization of radiation belt electrons by ring current ion  
479 driven ULF waves, *J. Geophys. Res.*, 113, A02201, doi:10.1029/2007JA012468.

480 Ozeke, L. G., Mann, I. R., Murphy, K. R., Rae, I. J., Milling, D. K., Elkington, S. R., . . . Singer,  
481 H. J. (2012). ULF wave derived radiation belt radial diffusion coefficients. *Journal of*  
482 *Geophysical Research: Space Physics*, 117 (4). doi:10.1029/2011JA017463

483 Ozeke, L. G., I. R. Mann, K. R. Murphy, A. W. Degeling, S. G. Claudpierre and H. E. Spence  
484 (2018), Explaining the apparent impenetrable barrier to ultra-relativistic electrons in the outer  
485 Van Allen belt, *Nature Comms.* 9, 1844.

486 Press, W. (1992). Numerical recipes in C: The art of scientific computing, no. bk. 4 in numerical  
487 recipes in C : the art of scientific computing. New York, NY, USA: William H. Press,  
488 Cambridge University Press.

489 Louis G. Ozeke, Ian R. Mann, Kyle R. Murphy, Alex W. Degeling, Seth G. Claudepierre &  
490 Harlan E. Spence (2018), Explaining the apparent impenetrable barrier to ultra-relativistic  
491 electrons in the outer Van Allen belt, *Nature Communications*, volume 9, Article number: 1844

492 Rae, I. J., Mann, I. R., Murphy, K. R., Ozeke, L. G., Milling, D. K., Chan, A. A., . . . Honary, F.  
493 (2012). Ground-based magnetometer determination of in situ Pc4-5 ULF electric field wave  
494 spectra as a function of solar wind speed. *Journal of Geophysical Research: Space Physics*, 117  
495 (4). doi:10.1029/2011JA017335

496 Rae, I. J., Murphy, K. R., Watt, C. E. J., & Mann, I. R. (2011). On the nature of ULF wave  
497 power during nightside auroral activations and substorms: 2. Temporal evolution. *Journal of*  
498 *Geophysical Research: Space Physics*, 116 (1). doi:10.1029/2010JA015762

499 Rae, I.J., Murphy, K. R., Watt, C. E. J., Halford, A. J., Mann, I. R., Ozeke, L. G., Sibeck, D. G.,  
500 Clilverd, M. A., Rodger, C. J., Degeling, A. W., Forsyth, C. and Singer, H. J. (2018) The role of  
501 localised compressional Ultra-Low Frequency waves in energetic electron precipitation. *Journal*  
502 *of Geophysical Research: Space Physics*, 123 (3). pp. 1900-1914. ISSN 2169-9402 doi:  
503 10.1002/2017ja024674

504 G.D. Reeves, H.E. Spence, M.G. Henderson, R.H.W. Friedel, H.O. Funsten, D.N. Baker, S.G.  
505 Kanekal, J.B. Blake, J.F. Fennell, S.G. Claudepierre, R.M. Thorne, D.L. Turner, C.A. Kletzing,  
506 W.S. Kurth, B.A. Larsen, J.T. Niehof, S.K. Morley (2013), Electron acceleration in the heart of  
507 the Van Allen radiation belts, *Science*, 341(6149):991-4. doi: 10.1126/science.1237743

508 Sandhu, J. K., Yeoman, T. K., James, M. K., Rae, I. J., & Fear, R. C. (2018a). Variations of  
509 high-latitude geomagnetic pulsation frequencies: A comparison of time-of-flight estimates and  
510 IMAGE magnetometer observations. *Journal of Geophysical Research: Space Physics*, 123, 567–  
511 586. <https://doi.org/10.1002/2017JA024434>

512 Sandhu, J. K., Yeoman, T. K., & Rae, I. J. (2018b). Variations of Field Line Eigenfrequencies  
513 With Ring Current Intensity. *Journal of Geophysical Research: Space Physics*.  
514 doi:10.1029/2018JA025751

515 Sandhu, J. K., Rae, I. J., Freeman, M. P., Forsyth, C., Gkioulidou, M., Reeves, G. D., et al.  
516 (2018c). Energization of the ring current by substorms. *Journal of Geophysical Research: Space  
517 Physics*, 123, 8131–8148. <https://doi.org/10.1029/2018JA025766>

518 Samson, J. C., J. A. Jacobs, and G. Rostoker, Latitude dependent characteristics of long-period  
519 geomagnetic pulsations, *J. Geophys. Res.*, 76, 3675, 1971.

520 Shen, C., et al. (2014), Direct calculation of the ring current distribution and magnetic structure  
521 seen by Cluster during geomagnetic storms, *J. Geophys. Res. Space Physics*, 119, 2458–2465,  
522 doi:10.1002/2013JA019460.

523 Shue, J.-H., et al. (1998), Magnetopause location under extreme solar wind conditions, *J.  
524 Geophys. Res.*, 103(A8), 17691–17700, doi:10.1029/98JA01103.

525 Sibeck, D.G., Baumjohann, W., Elphic, R.C., Fairfield, D.H., Fennell, J.F. (1989), The  
526 magnetospheric response to 8--minute period strong--amplitude upstream pressure variations, *J.  
527 Geophys. Res.*, 94(a3), 2505–2519

528 Spence, H. E., G. D. Reeves, D. N. Baker, J. B. Blake, M. Bolton, S. Bourdarie, A. H. Chan, S.  
529 G. Claudpierre, J. H. Clemons, J. P. Cravens, S. R. Elkington, J. F. Fennell, R. H. W. Friedel,  
530 H. O. Funsten, J. Goldstein, J. C. Green, A. Guthrie, M. G. Henderson, R. B. Horne, M. K.  
531 Hudson, J.-M. Jahn, V. K. Jordanova, S. G. Kanekal, B. W. Klatt, B. A. Larsen, X. Li, E. A.  
532 MacDonald, I. R. Mann, J. Niehof, T. P. O'Brien, T. G. Onsager, D. Salvaggio, R. M. Skoug, S.  
533 S. Smith, L. L. Suther, M. F. Thomsen, and R. M. Thorne (2013), Science Goals and Overview  
534 of the Energetic Particle, Composition, and Thermal Plasma (ECT) Suite on NASA's Radiation  
535 Belt Storm Probes (RBSP) Mission, *Space Science Reviews*, doi:10.1007/s11214-013-0007-5.

536 Thorne, R. M., et al. (2013), Evolution and slow decay of an unusual narrow ring of relativistic  
537 electrons near  $L \sim 3.2$  following the September 2012 magnetic storm, *Geophys. Res. Lett.*, 40,  
538 3507–3511, doi:10.1002/grl.50627.

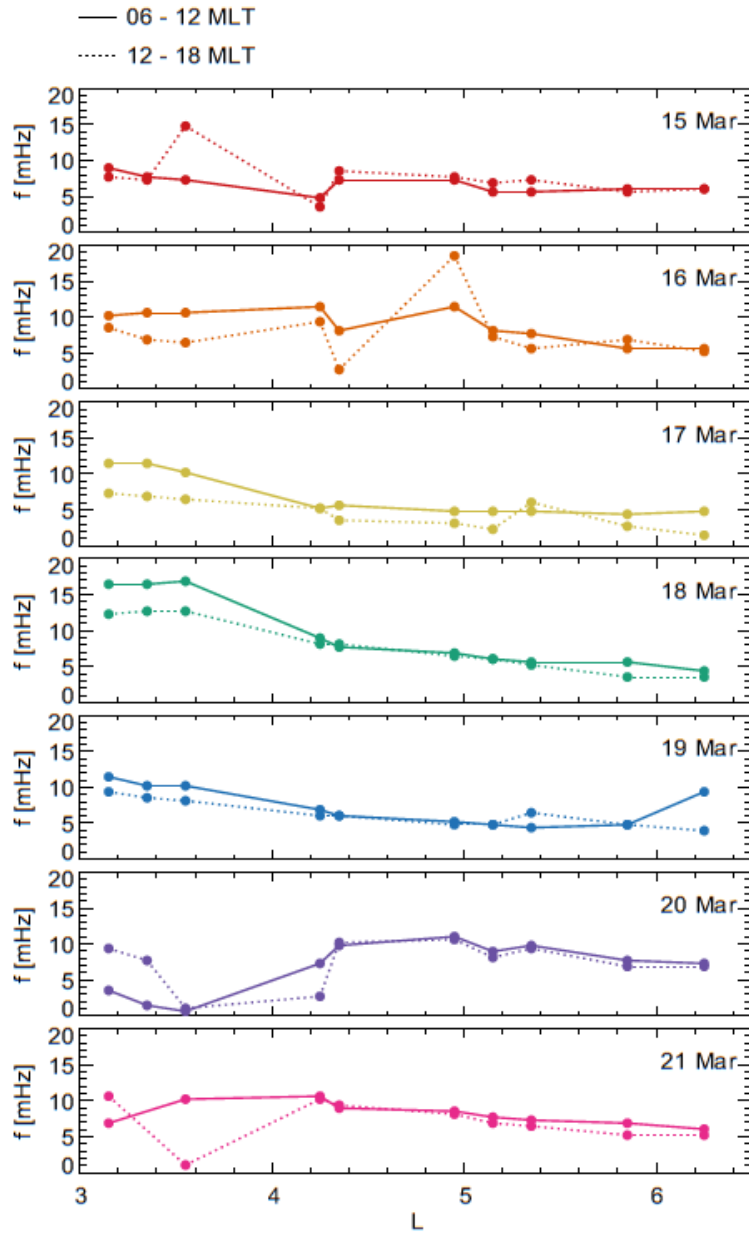
539 Tu, W., G. S. Cunningham, Y. Chen, M. G. Henderson, E. Camporeale, and G. D. Reeves  
540 (2013), Modeling radiation belt electron dynamics during GEM challenge intervals with the  
541 DREAM3D diffusion model, *J. Geophys. Res. Space Physics*, 118, 6197–6211,  
542 doi:10.1002/jgra.50560.

543 Waters, C. L., F. W. Menk, and B. J. Fraser (1991), The resonance structure of low latitude Pc3  
544 geomagnetic pulsations, *Geophys. Res. Lett.*, 18(12), 2293–2296.

545 Waters, C. L., J. C. Samson, and E. F. Donovan (1995), The temporal variation of the frequency  
546 of high latitude field line resonances, *J. Geophys. Res.*, 100(A5), 7987–7996.

547 Watt, C. E. J., Rae, I. J., Murphy, K. R., Anekallu, C., Bentley, S., & Forsyth, C. (2017). The  
548 parameterization of wave-particle interactions in the Outer Radiation Belt. *Journal of*  
549 *Geophysical Research: Space Physics*. doi:10.1002/2017JA024339

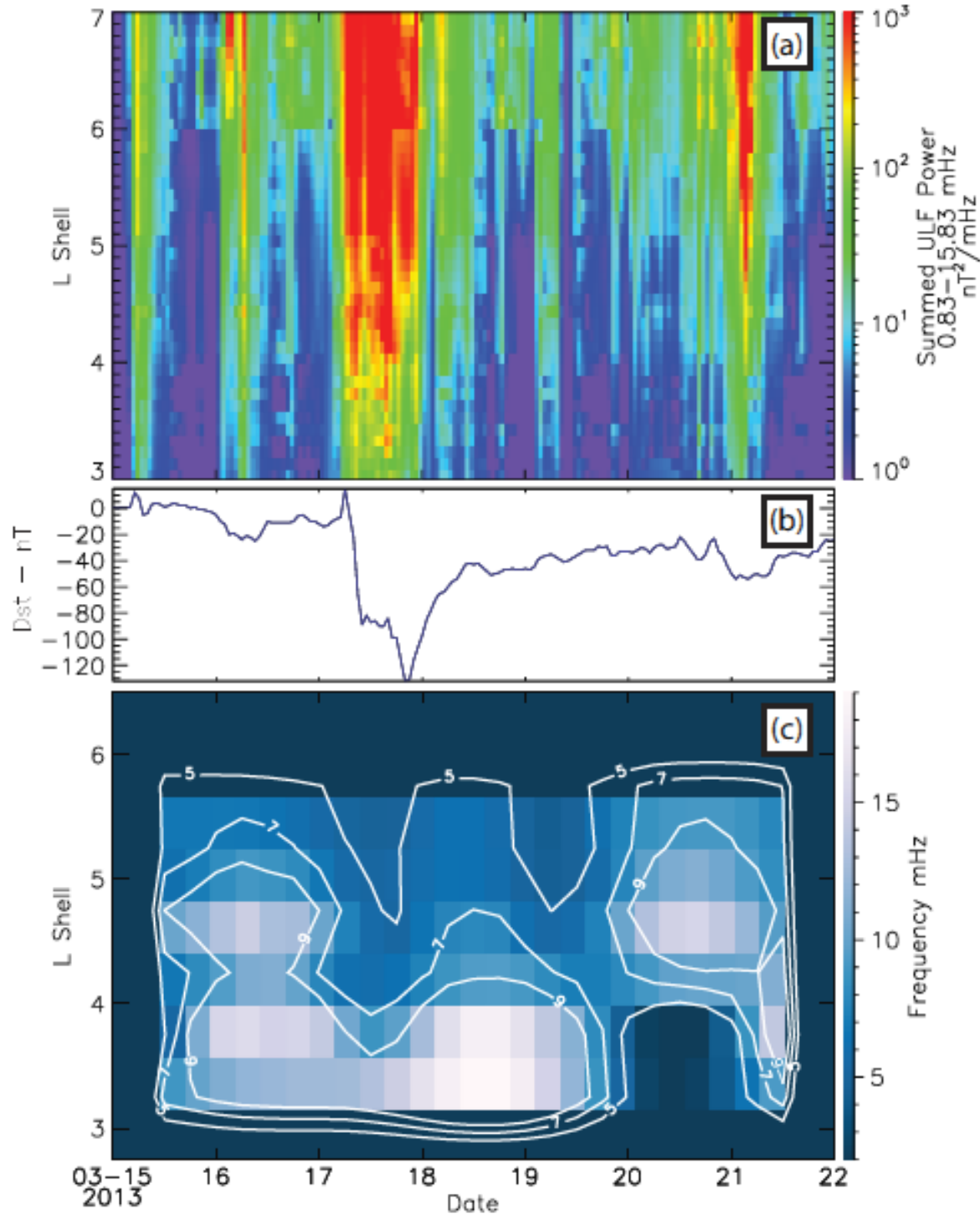
550 A.W. Yau, W.K. Peterson, E.G. Shelley (1988), Quantitative parametrization of energetic  
551 ionospheric ion outflow, in *Modeling Magnetospheric Plasma*, ed. by T.E. Moore et al..  
552 *Geophys. Monogr. Ser.*, vol. 44 (AGU, Washington D.C.), pp. 211–217  
553



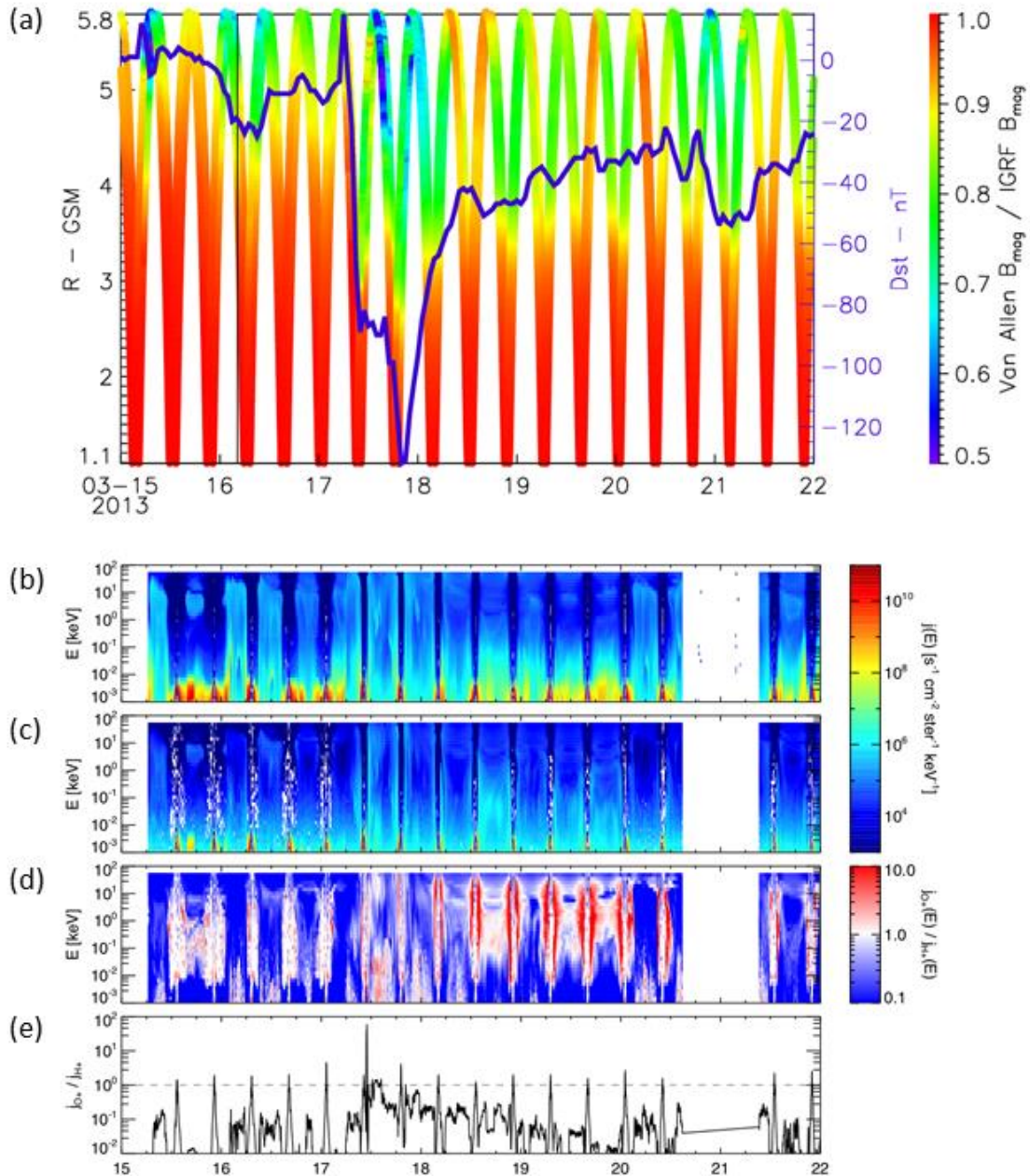
554

555 **Figure 1.** Eigenfrequency profiles from the CARISMA magnetometer array “Churchill Line”  
 556 (see Supplementary S2). Figure 1 contains the cross-phase results using the automated algorithm  
 557 from Sandhu et al. [2018a] from measurements from station pairs shown in Supplementary  
 558 Material S2.

559



560  
561 **Figure 2.** (top) Summed ULF wave power from the IMAGE and CARISMA magnetometer  
562 chains for the 15-22 March 2013 storm over the dayside magnetosphere (06-18 MLT)  
563 interpolated onto a 2D grid with 1hour resolution and 0.1L step (original data in Supplementary  
564 Material S2). (bottom) a 2D interpolation with 6 hours in time and 0.25 L spatial scales of the  
565 Alfvén continuum shown in Figure 1.  
566



567  
568  
569  
570  
571  
572  
573  
574  
575  
576

**Figure 3.** (a) Comparison between observed field magnitude from Van Allen Probes A and B and the International Geomagnetic Reference Field (IGRF) field model. Figure 3(a) shows the ratio of observed magnitude to IGRF magnitude as a function of radial distance and time. Overplotted on the right axis is the Dst index. Figure 3(b-e). HOPE observations of omnidirectional energy flux for H<sup>+</sup> ions,  $j_{\text{H}^+}(E)$ , and O<sup>+</sup> ions,  $j_{\text{O}^+}(E)$ , averaged at 5 minute resolution from 15 - 22 March 2015. Figure 3 (b,c) energy spectrograms of  $j_{\text{H}^+}(E)$  and  $j_{\text{O}^+}(E)$ , respectively. (d) energy spectrogram showing the ratio of  $j_{\text{O}^+}(E)$  to  $j_{\text{H}^+}(E)$ . (e) the ratio of  $j_{\text{O}^+}(E)$  to  $j_{\text{H}^+}(E)$  summed over all energies shown in Figure 3 (d).

**Figure 1.**

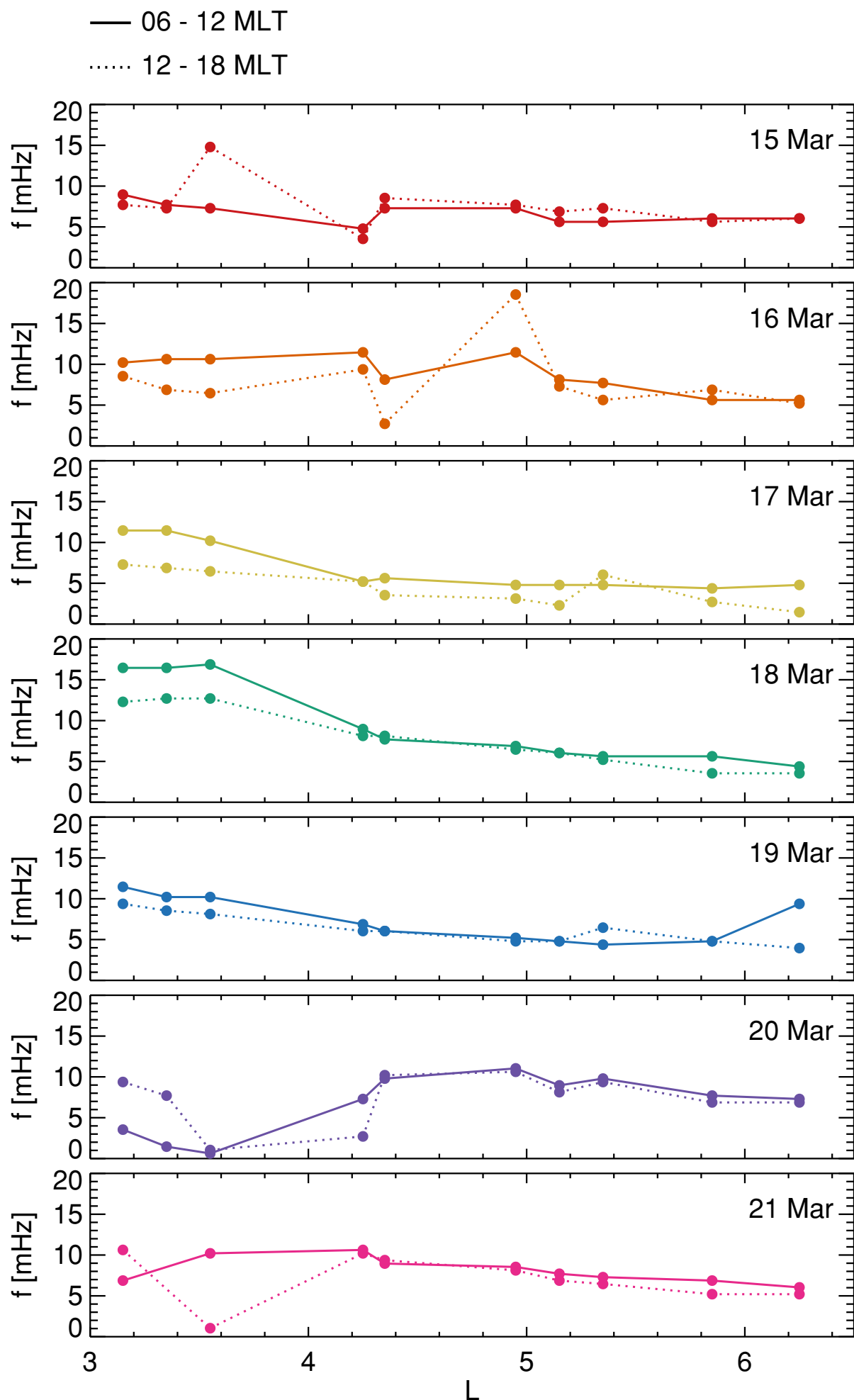


**Figure 2.**

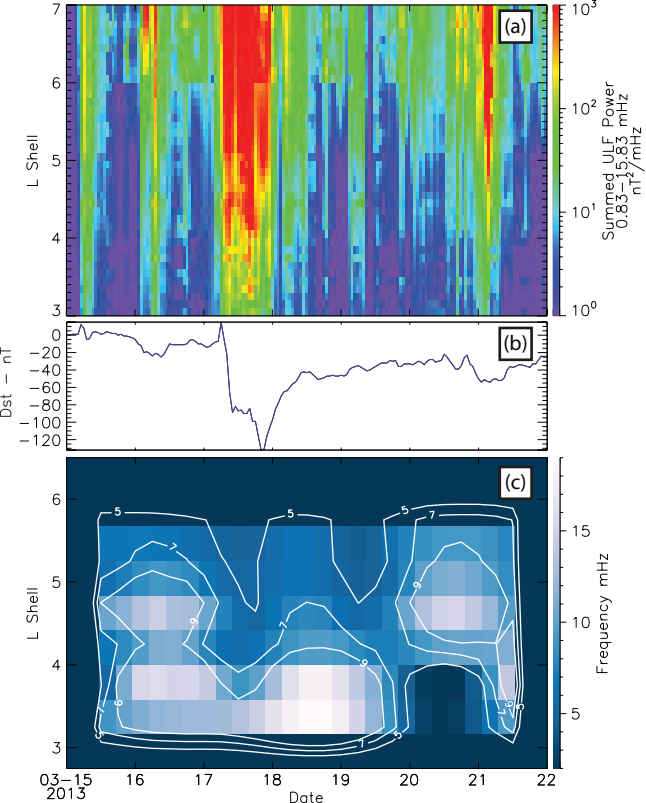


**Figure 3.**

